J. Fluid Mech. (2022), *vol*. 949, A11, doi:10.1017/jfm.2022.748

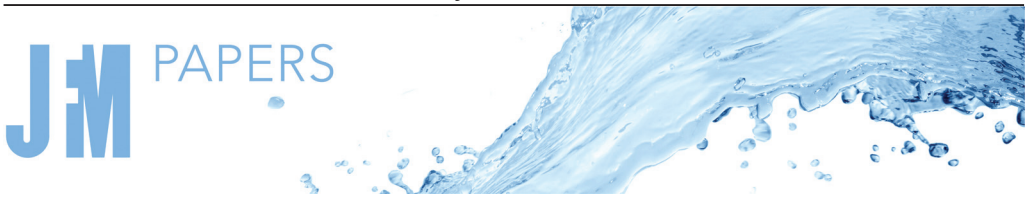

Vertical and torsional vibrations before the collapse of the Tacoma Narrows Bridge in 1940

Daeun Song[1], Woojin Kim[1], Oh-Kyoung Kwon[2] and Haecheon Choi[1,3,†]

[1]Department of Mechanical Engineering, Seoul National University, Seoul 08826, Korea

[2]Korea Institute of Science and Technology Information, Daejeon 34141, Korea

[3]Institute of Advanced Machines and Design, Seoul National University, Seoul 08826, Korea

(Received 1 November 2021; revised 26 August 2022; accepted 28 August 2022)

We perform a three-dimensional direct numerical simulation of flow over the Tacoma Narrows Bridge to understand the vertical and torsional vibrations that occurred before its collapse in 1940. Real-scale structural parameters of the bridge are used for the simulation. The Reynolds number based on the free-stream velocity and height of the deck fence is lower ($Re = 10\ 000$) than the actual one on the day of its collapse ($Re = 3.06 \times 10^6$), but the magnitude of a fluid property is modified to provide the real-scale aerodynamic force and moment on the deck. The vertical and torsional vibrations are simulated through two-way coupling of the fluid flow and structural motion. The vertical vibration occurs from the frequency lock-in with the vortex shedding, and its wavelength and frequency agree well with the recorded data in 1940. After saturation of the vertical vibration, a torsional vibration resulting from the aeroelastic fluttering grows exponentially in time, with its wavelength and frequency in excellent agreement with the recorded data of the incident. The critical flutter wind speed for the growth of torsional vibration is obtained as $3.56 < U_c/(f_{nat}B) \leq 4$, where U_c is the critical flutter wind speed, f_{nat} is the natural frequency of the torsional vibration and B is the deck width. Finally, apart from the actual vibration process in 1940, we perform more numerical simulations to investigate the roles of the free-stream velocity and vertical vibration in the growth of the torsional vibration.

Key words: flow-structure interactions, separated flows

1. Introduction

On 7 November 1940, the Tacoma Narrows Bridge (TNB) collapsed only four months after it was opened. In the early morning, the bridge deck showed a vertical vibration with a wavelength of $2L_z/9$ or $L_z/5$ at a frequency of 0.60–0.63 Hz, where L_z is the length of

† Email address for correspondence: choi@snu.ac.kr

the bridge deck. The vertical vibration changed abruptly to a torsional one around 10:00, and the bridge oscillated at 0.23 Hz with the angular amplitude reaching up to 45 degrees right before the collapse at 11:00 (Ammann, von Kármán & Woodruff (1941); see also Olson, Wolf & Hook (2015) for a brief summary of the incident).

The main cause of the collapse has been widely attributed to resonance; i.e. the natural frequency of the bridge is connected to the frequency of the Kármán vortex shedding, leading to the failure of the bridge. For example, an undergraduate fluid mechanics textbook by White (2016) says 'Resonance can occur if a vortex-shedding frequency is near a body's structural vibration frequency. . . . A striking example is the disastrous failure of the Tacoma Narrows suspension bridge in 1940, when wind-excited vortex shedding caused resonance with the natural torsional oscillations of the bridge'. Similar statements can be found in other engineering and physics textbooks (Den Hartog 1985; Serway & Jewett 2018). However, Scanlan (1982) indicated by referring to von Kármán & Edson (1967) and Yakubovich & Starzhinskii (1975) that the torsional oscillatory behaviour of the bridge did not match that of the naturally shed vortex street, and claimed that the TNB underwent an aeroelastic separated-flow fluttering right before the collapse. Later, Billah & Scanlan (1991) showed that the frequency of the torsional vibration was considerably different from that of the vortex-shedding frequency ($\sim$1 Hz), and indicated that the torsional fluttering of the bridge, which led the bridge to its collapse, was the result of an aerodynamically induced 'self-excitation', as opposed to an external excitation (see also Zhang, Dou & Gao 2020). They affirmed that the vortex shedding is an essential ingredient for the fluttering to occur. However, as pointed out by Larsen (2000), they were unable to directly associate the vortex motion with the appearance of negative damping (note that the onset of dynamic instability due to the accumulation of energy is referred to as negative damping, as opposed to positive damping by which energy is dissipated away from the system).

To reveal the contribution of vortex motion to the torsional instability, Larsen (2000) studied the instability mechanism of the H section of the TNB deck. The procedure of the deck receiving net work from the flow as vortices emerge at the leading edge and drift toward the trailing edge according to the deck oscillation was provided in detail. A critical wind speed obtained for the onset of the torsional instability was $U_c \approx 4fB$, where f is the prescribed frequency of the deck cross-section oscillation and B is the deck cross-section width. For U(wind speed) $< U_c$, the net work done to the bridge by the vortices was negative and thus the oscillatory motion was damped (positive damping), but for $U \geq U_c$, the damping switches to negative, leading to an increase in the torsional amplitude and the onset of torsional instability. The wind speed during the vibration and collapse of the TNB in 1940 ($U \approx 8fB$) was higher than the critical wind speed, and thus the bridge was torsionally unstable. Green & Unruh (2006) further improved this result by considering the growth and reattachment of the vortices.

In contrast to the claim that the cause of the torsional vibration is aeroelastic, studies based on nonlinear structure models (see Lacarbonara (2013) for general introduction to the nonlinear structural mechanics) have shown that the torsional instability of the bridge is mainly a structural phenomenon, and attributed the dynamic instability of the bridge to large vertical oscillations. McKenna (1999) derived a simple nonlinear two-dimensional model of a system with vertical and torsional oscillations and demonstrated a rapid transition of a large vertical vibration to torsional vibration only under the condition where a periodic torsional force was assigned. Berchio & Gazzola (2015) and Arioli & Gazzola (2015) provided a nonlinear model of a system (without any aerodynamic effect) and showed that, during a large vertical vibration, energy of the vertical mode is transferred to

a torsional mode and torsional vibration suddenly appears. They showed the existence of an energy threshold, over which the bridge became torsionally unstable. Later, Arioli & Gazzola (2017) suggested a more refined nonlinear model for suspension bridges in which the role of cables is also included into the nonlinearity of the system (again without any aerodynamic effect) and obtained the energy threshold of instability according to each vertical mode using the structural parameters and length scales of the TNB. They showed that the failure of the TNB was neither due to the resonance of the structure by the Kármán vortex street, nor due to pure aeroelasticity. However, their simulation did not consider the aerodynamic effect of the wind, and thus an initial condition was required to initiate the vertical vibration of the bridge.

So far, most of numerical studies have been limited to two-dimensional analyses (Billah & Scanlan 1991; McKenna 1999; Larsen 2000; Green & Unruh 2006; Adekanye & Washington 2018) or to purely structural simulations (McKenna 1999; Arioli & Gazzola 2015, 2017; Berchio & Gazzola 2015; Adekanye & Washington 2018). In those studies, how the vibration was initiated was not investigated but an initial vibration was prescribed. Previous experimental studies (Ammann *et al.* 1941; Scanlan & Tomko 1971; Hu, Zhao & Ge 2022) and numerical ones employing three-dimensional fluid–structure interaction (Szabó, Györgyi & Kristóf 2020) also prescribed the initial motions of the bridge models. Abbas, Kavrakov & Morgenthal (2017) summarized the aerodynamic analysis techniques and numerical and experimental methods for flutter stability analysis of long-span cable-supported bridges.

As the wind is essential to the initiation of the vibration from the wind–bridge interaction and the vibration switches from vertical to torsional, an unsteady three-dimensional numerical simulation together with fluid–structure interaction is necessary to investigate the vibration mechanism. Therefore, in the present study, we perform a direct numerical simulation of the flow over a vibrating TNB together with solving the structure equations suggested by Arioli & Gazzola (2017), to describe the vertical and torsional vibrations that occurred before the collapse of the TNB in 1940. We start the simulation in the presence of the free-stream velocity with a static condition of the TNB. Then, its vertical vibration and transition to torsional vibration occur. The Reynolds number considered is $Re = 10\ 000$ based on the free-stream velocity and height of the deck fence. This Reynolds number is much lower than the real one, $Re = 3.06 \times 10^6$, but the realistic aerodynamic force and moment on the TNB are computed by modifying the magnitude of a fluid property (see § 2). Modal analyses are also conducted to identify the resonance modes of the vertical and torsional vibrations. A few more numerical simulations are also conducted to find the critical flutter wind speed and to examine the roles of the free-stream velocity and vertical vibration in the growth of the torsional vibration. The numerical details are given in § 2, and the behaviours of the vertical and torsional vibrations are discussed in detail in § 3, followed by conclusions in § 4.

2. Numerical methods

The governing equations for unsteady three-dimensional incompressible flow with a fluid–structure interface are solved in Eulerian coordinates, while the nonlinear dynamic equations for the TNB (Arioli & Gazzola 2017) with the aerodynamic force and moment at the interface are solved in Lagrangian coordinates. A weak-coupling approach for the fluid–structure interaction (Kim, Lee & Choi 2018) is employed (see below for details).

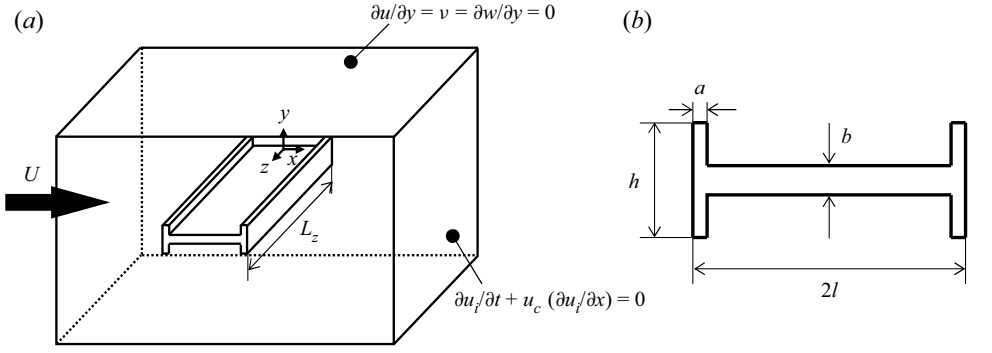

Figure 1. Computational domain and deck geometry: (*a*) computational domain; (*b*) cross-section of the deck.

2.1. *Fluid flow*

The governing equations for the fluid flow are the unsteady three-dimensional incompressible Navier–Stokes and continuity equations, and their non-dimensional forms are

$$\frac{\partial u_i}{\partial t} + \frac{\partial u_i u_j}{\partial x_j} = -\frac{\partial p}{\partial x_i} + \frac{1}{Re}\frac{\partial^2 u_i}{\partial x_j \partial x_j} + f_i, \tag{2.1}$$

$$\frac{\partial u_i}{\partial x_i} - q = 0, \tag{2.2}$$

where $x_i(= x, y, z)$ is the Cartesian coordinates, $u_i(= u, v, w)$ is the corresponding velocity, p is the pressure and f_i and q are the momentum forcing and mass source/sink used for the immersed-boundary method, respectively (see Kim, Kim & Choi (2001) for details). The free-stream velocity (U) and deck-fence height (h) are used for the non-dimensionalization (figure 1). The Reynolds number is defined as $Re = \rho_f U h/\mu_f$, where ρ_f and μ_f are the fluid density and viscosity, respectively. We perform direct numerical simulation, i.e. without using any turbulence model. The wind speed during the collapse of the TNB in 1940 was 18 m s^{-1}, and thus the actual Reynolds number was $Re = 3.06 \times 10^6$. This Reynolds number is too high to handle using direct numerical simulation because of very long TNB deck length ($L_z = 853.44$ m). Instead of handling this actual Reynolds number, we rather perform a simulation at a much lower Reynolds number of $Re = 10\,000$ by modifying the magnitude of a fluid property. Justification of using a lower Reynolds number is following: (i) as the flow separation is fixed at the leading edge of the deck fence, the Strouhal number ($St = f_{vs}h/U$, where f_{vs} is the vortex-shedding frequency) and drag coefficient ($C_D = D/(0.5\rho_f U^2 h L_z)$, where D is the drag force) vary little with the Reynolds number for a wide range of the Reynolds number (Schew 2013); (ii) the aerodynamic force and moment on a bluff body are mostly determined by the inertia of the flow (i.e. pressure distribution on the body) rather than by the skin friction. Therefore, even though the computation is carried out at a lower Reynolds number, we maintain the fluid density as that of air ($\rho_f = 1.247$ kg m^{-3}) but change the viscosity to be $\mu_f = 5.387 \times 10^{-3}$ N s m^{-2} to match the Reynolds number as 10 000. Then, the drag force can be reasonably computed by providing the actual air density ($D = C_D \times 0.5\rho_f U^2 h L_z$) and neglecting the effect of the viscosity.

An implicit fractional step method (Choi & Moin 1994) with linearization (Kim, Baek & Sung 2002) is used for time advancement of (2.1) and (2.2). The second-order central

h	height of the deck fence	2.4 m
L_z	length of the deck	$355.6h$
l	half width of the deck	$2.5h$
a	thickness of the railings	$0.05h$
b	thickness of the deck	$0.2214h$

Table 1. Deck parameters.

difference method is applied to all the spatial derivative terms in the framework of the finite volume method. The computational domain for the fluid flow and the geometry of the bridge deck are shown in figure 1. The hangers, cables and towers (see later in figure 3) are neglected and only the deck is considered for the computation of the fluid flow, because the deck is the main source of the vortex shedding which again produces the force and moment on the deck. Here, the x-, y- and z-axes are the streamwise, transverse and spanwise directions, respectively; $z = 0$ is located at one end of the deck, and $x = 0$ and $y = 0$ are the location of the static deck centre. The height of the deck fence is $h = 2.4$ m. The length of the deck, $L_z = 853.44$ m, is equal to the spanwise length of the computational domain, and the deck width is $2l = 12$ m. The thicknesses of the railings and deck are $a = 0.12$ m and $b = 0.5313$ m, respectively. The length scales of the deck parameters with respect to h are given in table 1.

The number of grid points for the flow simulation is $4097 \times 1601 \times 2049$ in the x, y and z directions in the Cartesian mesh, and the computational domain size is $[-20h,\ 40h] \times [-20h, 20h] \times [0,\ 355.6h]$. The grids in the z direction are uniformly distributed by $\Delta z = 0.1736h$, and a periodic boundary condition is applied in this direction. On the other hand, non-uniform grids are distributed in the x and y directions with minimum grid sizes of $\Delta x = \Delta y = 0.005h$, and the grid distribution in the x–y plane is shown in figure 2, in which uniform grids are distributed near the deck ($[-2.7h, 4h] \times [-2.5h, 2.5h]$), and non-uniform grids are given with contraction (upstream of the deck) and expansion (downstream) factors of 0.9915 and 1.0008 in the x direction and with an expansion factor of 1.013 (upward and downward) in the y direction. A Dirichlet boundary condition of $(U, 0, 0)$ is applied at the inflow boundary, while a Neumann boundary condition of $\partial u/\partial y = v = \partial w/\partial y = 0$ is applied at the top and bottom boundaries (see also Kim, Lee & Choi (2016), Kim & Choi (2019) and Jin, Wu & Choi (2021) who used this boundary condition). A convective boundary condition, $\partial u_i/\partial t + u_c \partial u_i/\partial x = 0$, is applied at the outflow boundary to allow the vortices to exit the computational domain smoothly (Pauley, Moin & Reynolds 1990), where u_c is the instantaneous streamwise velocity averaged over the outflow boundary. The initial condition for the simulation is given as $(u/U, v/U, w/U) = (1, 0, 0)$, and a constant CFL (Courant–Friedrichs–Lewy) number of 2 is employed throughout the computation. We performed an additional simulation using coarser grids with $\Delta x = \Delta y = 0.007h$, and obtained the same frequencies and wavelengths of the vertical and torsional vibrations as those from the present grids, although the small-scale flow structures were slightly different. We also conducted a simulation with a larger computational time step size by fixing CFL$= 3$ during a torsional vibration period, and obtained nearly the same sectional lift and moment coefficients and the vertical and angular displacements as those from CFL$= 2$.

Owing to the large number of grids used for flow simulation, up to 2500 nodes of an Intel Xeon Phi 7250, which corresponds to 160 000 MPI (message-passing interface) processes, are used for the computation. Two-dimensional domain decomposition is applied to relieve

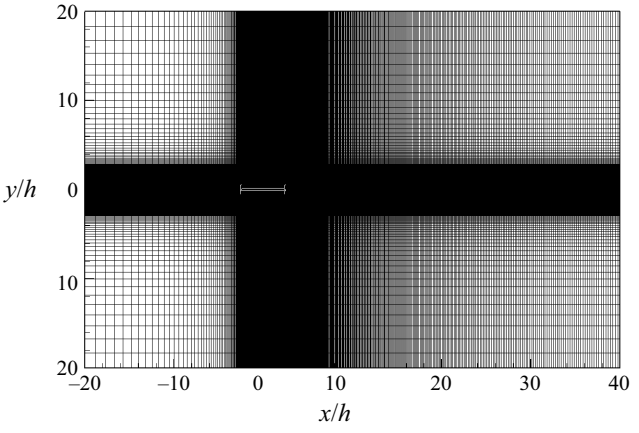

Figure 2. Grid distribution in an x–y plane. Here, every eighth grid point is plotted in each direction.

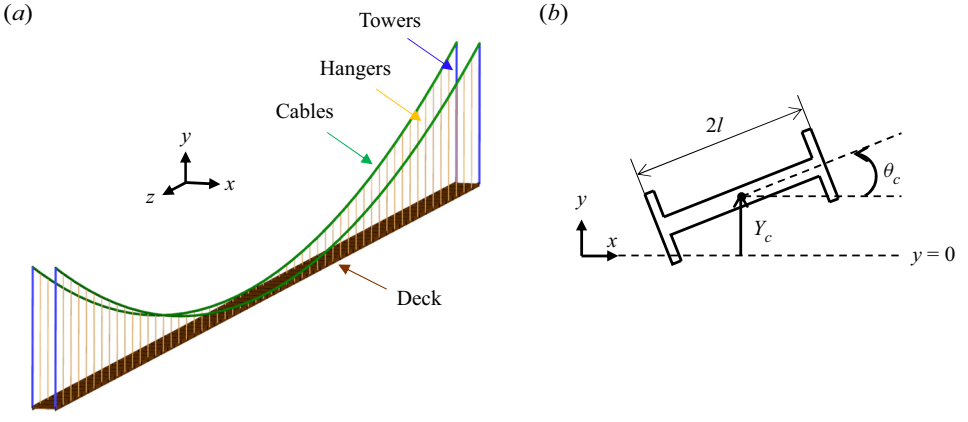

Figure 3. Description of the bridge structure: (*a*) cables, hangers, towers and deck of the TNB; (*b*) vertical displacement Y_c and rotational angle θ_c of a deck element.

the enormous computational load (Kwon *et al.* 2020), and a parallel TDMA (tridiagonal matrix algorithm) method (Kim *et al.* 2021) is employed to accelerate the computation.

2.2. *Structure vibration*

The vertical and rotational movements of a suspension bridge follow a nonlinear model proposed by Arioli & Gazzola (2017). In this model, the hangers are considered as a continuum connecting the cables and deck and their elastic deformation is neglected, while the tension by the cables is taken into account. The deck is divided into 2048 elements in the z direction, the same as the computational grids used for fluid flow in § 2.1. Each element of the deck is assumed to be rigid but to move in the y direction and rotate on the x–y plane (Arioli & Gazzola 2017). Thus, the vertical displacement and rotational angle are functions of z and t, i.e. $Y_c(z, t)$ and $\theta_c(z, t)$ (figure 3). In this figure, 2 cables, 110 hangers (which are treated as a continuous membrane on each side during simulation), 4 towers and a deck are shown.

The governing equations for a deck element are as follows:

$$(M+2m\xi)\,Y_{c_{tt}} = -EIY_{c_{zzzz}} + H_0\left\{\frac{2Y_{c_z}}{\xi^2} - 3\frac{s'(Y_{c_z}^2+l^2\theta_{c_z}^2)}{\xi^4}\right\}_z + \frac{AE}{L_c}\frac{s''}{\xi^3}\int_0^{L_z}\frac{Y_{c_z}^2+l^2\theta_{c_z}^2}{\xi^3}\,\mathrm{d}z - \frac{2AE}{L_c}\left(\frac{s'}{\xi}+\frac{Y_{c_z}}{\xi^3}\right)_z\int_0^{L_z}\frac{s''Y_c}{\xi^3}\,\mathrm{d}z - \frac{2AEl^2}{L_c}\left(\frac{\theta_{c_z}}{\xi^3}\right)_z\int_0^{L_z}\frac{s''\theta_c}{\xi^3}\,\mathrm{d}z + \frac{1}{2}\rho_f U^2 hC_{L_s}, \tag{2.3}$$

$$\left(\frac{M}{3}+2m\xi\right)\theta_{c_{tt}} = \frac{GK}{l^2}\theta_{c_{zz}} + 2H_0\left(\frac{\theta_{c_z}}{\xi^2} - 3\frac{s'Y_{c_z}\theta_{c_z}}{\xi^4}\right)_z + \frac{2AE}{L_c}\frac{s''}{\xi^3}\int_0^{L_z}\frac{Y_{c_z}\theta_{c_z}}{\xi^3}\,\mathrm{d}z - \frac{2AE}{L_c}\left(\frac{s'}{\xi}+\frac{Y_{c_z}}{\xi^3}\right)_z\int_0^{L_z}\frac{s''\theta_c}{\xi^3}\,\mathrm{d}z - \frac{2AE}{L_c}\left(\frac{\theta_{c_z}}{\xi^3}\right)_z\int_0^{L_z}\frac{s''Y_c}{\xi^3}\,\mathrm{d}z + \frac{1}{2}\rho_f U^2h^2\frac{C_{M_s}}{l^2}, \tag{2.4}$$

where the subscripts t and z indicate the time and spatial derivatives of the variables, $s(z)$ and $\xi(z)(=\sqrt{(1+s'^2)})$ are the location and local length of the cables at rest, respectively, and $A, E, G, H_0, I, K, L_c, M$ and m are listed in table 2. Here, $C_{L_s}(=2L_s/(\rho_f U^2 h))$ and $C_{M_s}(=2M_s/(\rho_f U^2 h^2))$ are the sectional lift and moment coefficients, respectively, where L_s and M_s are the sectional lift and moment, respectively. The structural damping is neglected in (2.3) and (2.4). The locations of the cables at rest are obtained by the following relation:

$$2H_0 s'' = \left(M + 2m\sqrt{1+s'^2}\right)g \text{ at } t=0, \tag{2.5}$$

where g is the gravitational acceleration. This equation shows the balance between the tension of the cables and the gravitational force of the deck and cables, but neglects the gravitational force of the hangers (Arioli & Gazzola 2017). The location of the cables at their ends are fixed to the four towers, i.e. $s(0) = s(L_z) = 30h$. The bridge is initially at rest ($Y_c = \theta_c = 0$) and the ends of the deck ($z = 0$ and L_z) are fixed at their original positions. Note that the governing equations (2.3) and (2.4) are slightly different from those in Arioli & Gazzola (2017), because in the latter the direction of the y coordinate is the opposite to that in the present study. The generalized-α method by Chung & Hulbert (1993) is used to solve (2.3) and (2.4) in time, and the second-order central difference method and trapezoidal method are used for the spatial derivative and integral terms, respectively.

The kinetic (E_{kin}) and gravitational (E_{grav}) energies of the deck and cables, the elastic energy of the deck (E_{el}), the energy required for each cable to deform under tension (E_c) and the energy required to change the cable length (E_{tc}) are given as follows (Arioli & Gazzola 2017):

$$E_{kin} = \frac{M}{2}\int_0^{L_z}\left(\frac{l^2\theta_{c_t}^2}{3} + Y_{c_t}^2\right)\mathrm{d}z + \frac{m}{2}\int_0^{L_z}({p_1}_t^2 + {p_2}_t^2)\xi\,\mathrm{d}z, \tag{2.6}$$

$$E_{grav} = Mg\int_0^{L_z} Y_c\,\mathrm{d}z + mg\int_0^{L_z}(p_1+p_2)\xi\,\mathrm{d}z, \tag{2.7}$$

A	cross-sectional area of the cable	0.1228 m^2
E	Young's modulus of the deck and cables	210 GPa
G	shear modulus of the deck	81 GPa
H_0	tension of the cables	58 300 kN
I	linear density of the moment of inertia of the cross-section of the deck	0.15 m^4
K	torsional constant of the deck	6.44×10^{-6} m^4
L_c	length of each cable	868.62 m
M	mass of the deck per unit length	7198 kg m^{-1}
m	mass of the cable per unit length	981 kg m^{-1}

Table 2. Material properties of the TNB parameters (from Arioli & Gazzola 2017).

$$E_{el} = \frac{EI}{2}\int_0^{L_z} Y_{czz}^2\,\mathrm{d}z + \frac{GK}{2}\int_0^{L_z}\theta_{cz}^2\,\mathrm{d}z, \tag{2.8}$$

$$E_c(p_i) = H_0\int_0^{L_z}\xi\left(\sqrt{1+(s'+p_{iz})^2}-\sqrt{1+s'^2}\right)\mathrm{d}z, \quad (i=1,2), \tag{2.9}$$

$$E_{tc}(p_i) = \frac{AE}{2L_c}\left(\int_0^{L_z}\sqrt{1+(s'+p_{iz})^2}\,\mathrm{d}z - L_c\right)^2 \quad (i=1,2), \tag{2.10}$$

where $p_1(z,t) = Y_c + l\theta_c$ and $p_2(z,t) = Y_c - l\theta_c$ are the displacements of two cables sharing a deck element with respect to its static position.

2.3. *Fluid–structure interaction*

A weak-coupling method by Kim *et al.* (2018) is used for fluid–structure interaction, in which the governing equations of the structure and fluid are solved alternatively in a staggered manner. First, the provisional displacement and velocity of the fluid–structure interface are obtained using the information obtained at the previous time step, and the velocity and pressure of the fluid at the current time step are updated with the provisional information. Then, the hydrodynamic force and moment on the interface are obtained from the flow field at the current time step, with which the velocity and acceleration of the structure are obtained. This method provides faster computation and easier implementation than a strong-coupling method does, while keeping a second-order accuracy. The detailed procedure is given in Kim *et al.* (2018). As we shall show below (§§ 3.2 and 3.3), with the present numerical methods, the frequency and wavelength of the vertical and torsional vibrations are in excellent agreement with those of the actual incident, and the critical flutter wind speed obtained also agrees well with those of previous experimental and numerical studies.

3. Results

In this section, the characteristics of the vertical and torsional vibrations are examined and compared with the recorded data of the incident of the TNB in 1940, and the critical flutter wind speed for the growth of the torsional vibration is obtained.

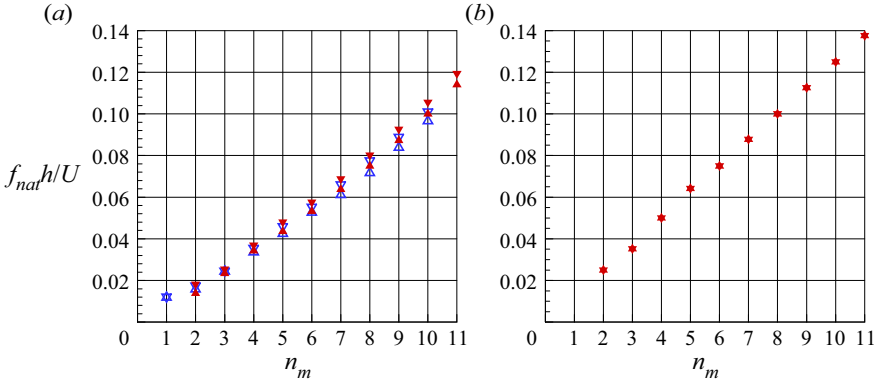

Figure 4. Variations of the natural frequencies of the TNB for the (*a*) vertical and (*b*) torsional vibrations: △ (blue), Arioli & Gazzola (2017) (initial energy at the energy threshold); ▽ (blue), Arioli & Gazzola (2017) (initial energy close to 0); ▲ (red), present (initial energy of 101.7 MJ for (*a*) and 1.90 GJ for (*b*)); ▼ (red), present (initial energy of 6.98 J for (*a*) and 19.0 J for (*b*)).

3.1. *Natural frequencies of the TNB*

The vertical and torsional vibration modes are obtained by separately solving (2.3) and (2.4) with $\theta_c = C_{L_s} \equiv 0$ in (2.3) and $Y_c = C_{M_s} \equiv 0$ in (2.4). The initial conditions are given as $Y_{c_t}(z, t = 0)/U = A_{n_m} \sin(n_m \pi z/L_z)$ and $Y_c(z, t = 0) = 0$ for the vertical modes, and $\theta_{c_t}(z, t = 0)h/U = B_{n_m} \sin(n_m \pi z/L_z)$ and $\theta_c(z, t = 0) = 0$ for the torsional modes, where $n_m = 1, 2, \ldots, 11$. To see if the vertical and torsional vibration modes depend on the initial energy level E (sum of (2.6)–(2.10)), we provide two different A_{n_m} values and B_{n_m} values: for the vertical vibration, $A_{n_m} = 0.0001$ and 0.4, resulting in $E = 6.98$ J and 101.7 MJ, respectively; for the torsional vibration, $B_{n_m} = 0.0001$ and 1, resulting in $E =$ 19.0 J and 1.90 GJ, respectively. Note that the total energy (E) does not change in time because there is no energy loss.

Figure 4 shows the variations of the natural frequencies f_{nat} with the vertical and torsional vibration wavenumbers n_m, together with those for the vertical vibration obtained by Arioli & Gazzola (2017). The natural frequency for the vertical vibration increases almost linearly with the wavenumber n_m and shows weak dependence on the initial energy, agreeing well with the result by Arioli & Gazzola (2017). A notable difference is that no natural frequency exists for $n_m = 1$ (wavelength of $2L_z$) from the present study, but Arioli & Gazzola (2017) obtained its natural frequency. Currently, we do not know the reason for this difference. The natural frequency for the torsional vibration also linearly increases with the wavenumber n_m but shows no dependence on the initial energy because (2.4) becomes linear with $Y_c = 0$. To obtain the vortex-shedding frequency of the flow over the 'stationary' deck, a separate three-dimensional numerical simulation with the periodic boundary condition in the z direction is conducted at the same Reynolds number of $Re = 10\,000$. Figure 5 shows the contours of the instantaneous spanwise vorticity around the stationary deck and energy spectra of the vertical velocity v at three different positions behind the deck. With the stationary deck, the flow shows a periodic alternating vortex shedding and the Strouhal number corresponding to the vortex-shedding frequency is $St = f_{vs}h/U = 0.111$. The same frequency is obtained for the fluctuating lift and moment coefficients as well. This Strouhal number closely matches the non-dimensional natural frequency of $f_{nat}h/U = 0.1$–0.105 at $n_m = 10$ (figure 4*a*), indicating that the vortex shedding behind a stationary deck triggers the natural frequency at $n_m = 10$ (wavelength of

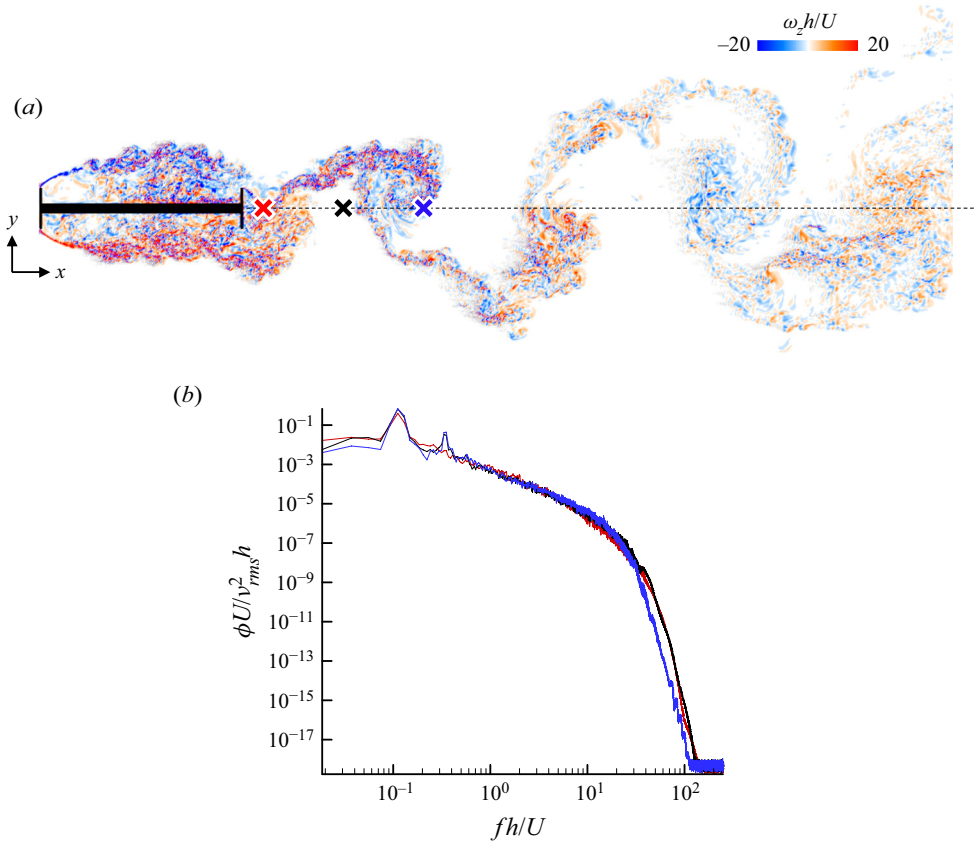

Figure 5. Flow over the stationary deck: (*a*) contours of the instantaneous spanwise vorticity; (*b*) energy spectra of the vertical velocity (v_{rms} is the root-mean-square vertical velocity fluctuations). In (*b*), ——— (red), $(x, y) = (3h, 0)$; ——— (black), $(5h, 0)$; ——— (blue), $(x, y) = (7h, 0)$. These locations are denoted as $\times$ in (*a*).

$\lambda_z = L_z/5$). This wavelength is similar to what was observed during the vertical vibration of the TNB (Ammann *et al.* 1941).

3.2. *Fluid–structure interaction*

Figure 6 shows the temporal behaviours of the vertical displacement and rotational angle at the deck centre along the span. At early time instants ($tU/h = 0 \sim 150$), the dominant wavelengths of Y_c and θ_c are $n_m = 1$ and 3 (see also figure 7). The occurrence of these wavelengths may be due to the abrupt start of the simulation ($u = U$, $v = 0$, and $w = 0$) at $t = 0$. The vertical vibration starts at $tU/h > 250$, and changes into a torsional vibration at $tU/h \approx 550$ (see below for more details). We show in § 3.3 that these early vibration patterns at $tU/h < 250$ are not required for the occurrence of the vertical vibration. As shown in figure 6(*c*), both the vertical displacement and rotational angle grow exponentially in time. However, unlike Y_c, θ_c is mainly composed of low wavenumber and frequency oscillations. For example, at $tU/h \leq 400$, Y_c contains both low and high wavenumber/frequency components, but θ_c has only low ones. At $tU/h = 500 \sim 600$, the high wavenumber/frequency components of Y_c disappear, and both Y_c and θ_c show very similar wavenumber/frequency characteristics at later time instants. To understand

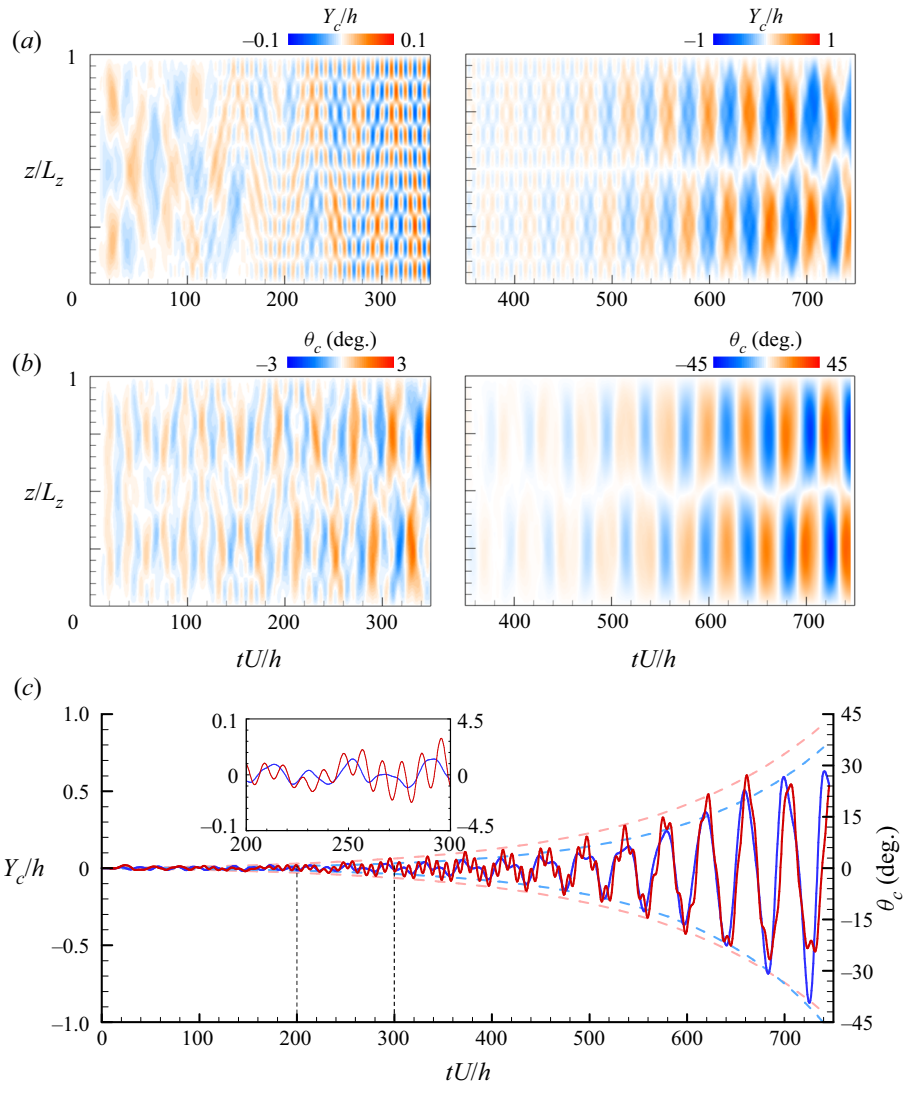

Figure 6. Temporal behaviours of the vertical displacement and rotational angle at the deck centre ($x = 0$): (*a*) Y_c; (*b*) θ_c; (*c*) Y_c (———, red) and θ_c (———, blue) at $z = L_z/4$. Note that the contour levels of the left and right figures in (*a*) and (*b*) are different. In (*c*), a zoom-in view of $Y_c(t)$ and $\theta_c(t)$ is given in $200 < tU/h < 300$.

the wavenumber characteristics of Y_c and θ_c, we perform their discrete sine transforms; i.e. Y_{c_j}/h (or θ_{c_j}) $= \sum_{n_m=0}^{N} a_{n_m} \sin(\pi n_m j \Delta z/L_z)$ for $j = 0, 1, 2, \ldots, N$ ($N = 2048$ and $\Delta z = L_z/N$), and the results are shown in figure 7. At $tU/h \approx 200$, Y_c contains the primary peak at $n_m = 10$, secondary peak at $n_m = 11$ and tertiary peak at $n_m = 2$, showing that the vertical vibration at this time contains both high and low wavenumber components. On the other hand, θ_c has the primary peak at $n_m = 1$ (rotational vibration) and secondary peak at $n_m = 7$, and non-negligible peaks at $n_m = 2$, 3 and 5, showing quite different wavenumber characteristics from Y_c. The primary peak of Y_c at $n_m = 10$ is closely associated with the vortex-shedding frequency. That is, the non-dimensional natural frequency of the deck at $n_m = 10$ is 0.1–0.105 (figure 4*a*), and this frequency is very similar to the vortex-shedding

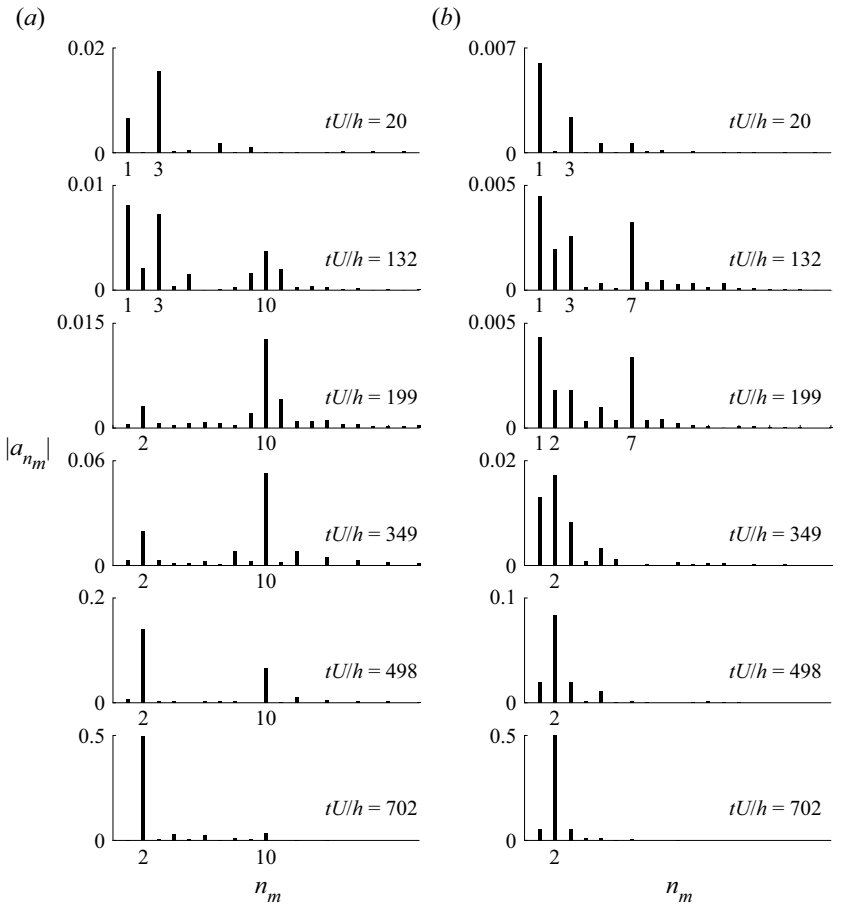

Figure 7. Coefficients of the discrete sine series of (*a*) Y_c and (*b*) θ_c at different time instants. Note that the scales of the vertical axes at different time instants are different.

frequency (figure 5*b*). In other words, at early time, the vertical vibration occurs in conjunction with the alternating vortex shedding. As time goes by, the contribution from $n_m = 2$ (torsional vibration) to Y_c increases and becomes dominant at $tU/h = 498$ and 702, so does to θ_c. Thus, Y_c and θ_c have the same dominant frequency with same phase (see figure 6*c*). Note that the torsional vibration occurs at the wavelength of L_z ($n_m = 2$), and its frequency is $fh/U = 0.025$, which is same as the natural frequency of θ_c at $n_m = 2$ ($f_{nat}h/U = 0.025$; figure 4*b*).

Figure 8 shows the temporal evolutions of the coefficients of the discrete sine series ($a_{n_m=2}$ and $a_{n_m=10}$) of Y_c and θ_c, respectively. Here, $|a_{n_m=10}|$ of Y_c exponentially grows until $tU/h \approx 400$ and decreases afterwards. On the other hand, $|a_{n_m=2}|$ values of both Y_c and θ_c grow exponentially even after the decrease of $|a_{n_m=10}|$ of Y_c. Note that, at $200 < tU/h < 400$, $|a_{n_m=10}|$ of Y_c is larger than $|a_{n_m=2}|$ of Y_c, indicating that the dominant wavelength of the vertical vibration at this time period is $\lambda_z = L_z/5$.

As both Y_c and θ_c grow and the vibration changes from the vertical to the torsional mode, it is interesting to know when the vibration mode changes. For this purpose, we

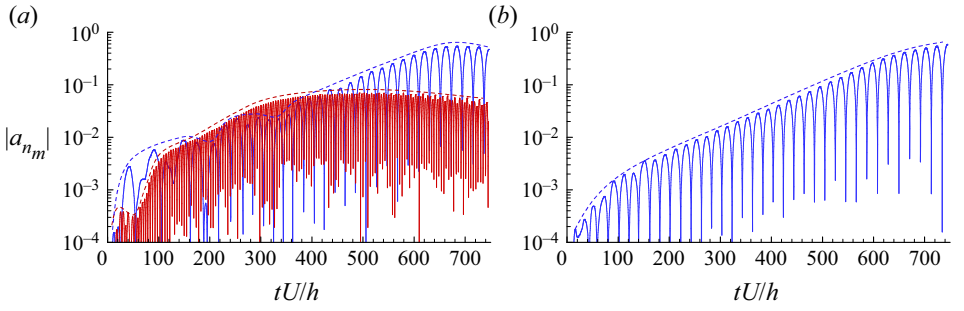

Figure 8. Temporal evolutions of the coefficients of the discrete sine series: (*a*) Y_c; (*b*) θ_c. Here, $|a_{n_m=2}|$ (———, blue) and $|a_{n_m=10}|$ (———, red).

define a non-dimensional variable Δ such as

$$\Delta(z,t) = (Y_{c_t}(z,t) + l\theta_{c_t}(z,t))(Y_{c_t}(z,t) - l\theta_{c_t}(z,t))/U^2, \tag{3.1}$$

where the quantities in the first and second parentheses are the velocities of the right and left fences, respectively (see figure 3*b*). The vertical vibration dominates when $\Delta > 0$, and the torsional vibration is dominant otherwise. Although this criterion does not perfectly describe the dominance of one vibration over the other, it at least qualitatively provides an idea as to which of the two vibrations is dominant. The contours of $\Delta(z,t)$ and span-averaged Δ, $\bar{\Delta}(t)$, are shown in figure 9. Starting from small negative values (possibly due to the abrupt start of the free-stream velocity at $t = 0$), $\Delta(z,t)$ is overall positive at $250 \leq tU/h < 450$, and then it is predominantly negative at $tU/h > 550$. Thus, this figure clearly shows the vertical vibration, transition from the vertical to torsional vibration, and torsional vibration.

Figure 10 shows the flow fields around the TNB at two different time instants corresponding to vertical and torsional vibrations. The flow separates from the left fence of the deck and vortices are shed alternately from the upper and lower sides, resulting in positive and negative lifts on the plate. At $tU/h = 354$, the wavelength of the vertical vibration is $\lambda_z = L_z/5$ (figures 6*a* and 10*c*) and the deck at the position of $z = L_z/4$ stays nearly horizontal ($\theta_{c_{max}} \simeq 3.3^\circ$ in figure 6*b*) and moves vertically (figures 10*a* and 10*c*). On the other hand, at $tU/h = 746$, the deck at the same spanwise position is significantly tilted, and a large leading edge vortex is formed on the lower side of the deck (figure 10*b*), causing strong aerodynamic moment on the deck. The wavelength of the torsional vibration is $\lambda_z = L_z$ (figure 10*c*). The peak frequencies of these vertical and torsional vibrations are $fh/U = 0.103$ (0.78 Hz) and 0.025 (0.19 Hz), respectively, which are similar to the recorded data (0.60–0.63 and 0.18 Hz, respectively) of Ammann *et al.* (1941) considering the uncertainty of the measurement at that time.

The temporal variations of the vertical displacement, rotational angle and sectional lift and moment coefficients at $z = L_z/4$ during $300 < tU/h < 700$ (including vertical and torsional vibration periods) are shown in figure 11. As shown in figure 11(*a*), during the vertical vibration ($300 < tU/h < 400$), the frequency of the rotational angle is noticeably different from that of the vertical displacement, whereas the rotational angle and vertical displacement are in phase during the torsional vibration ($tU/h > 500$). In figures 11(*b*) and 11(*c*), Y_c is in phase with C_{L_s} and C_{M_s} during the vertical vibration, but is 180° out of phase with C_{L_s} and 90° out of phase with C_{M_s} during the torsional vibration. On the other hand, θ_c has a lower frequency than that of C_{M_s} during the vertical vibration, but has the same frequency as that of C_{M_s} and is 90° out of phase with C_{M_s} during the

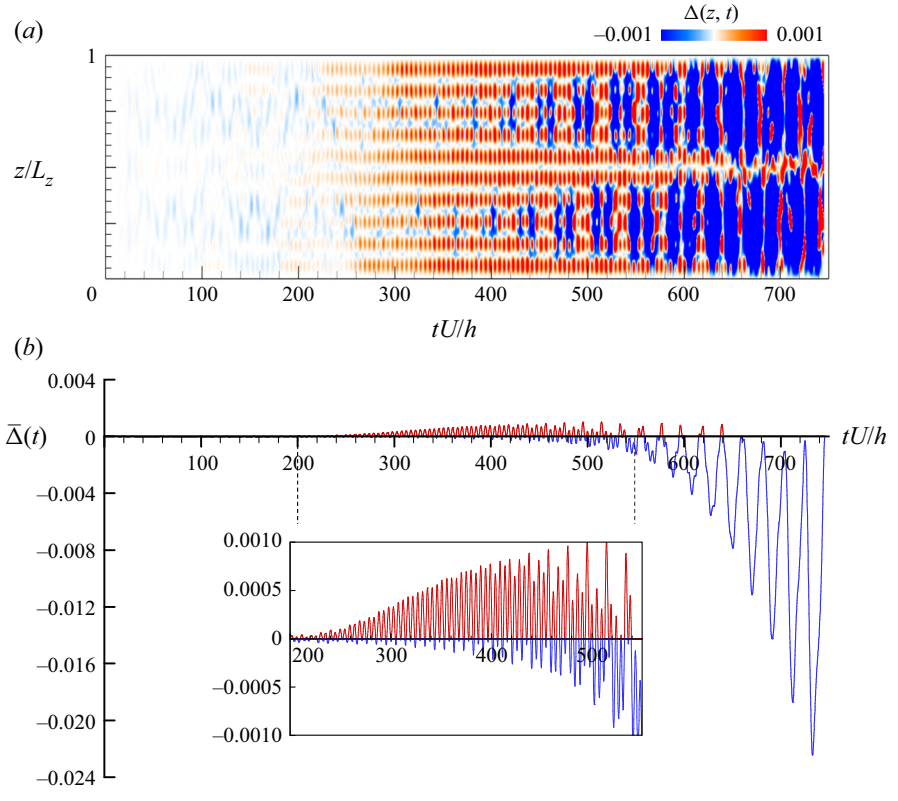

Figure 9. Relative strength of the vertical to torsional vibrations in time: (*a*) contours of $\Delta(z, t)$; (*b*) $\bar{\Delta}(t)$.

torsional vibration. This result indicates that the motion of the rotational angle, unlike the vertical displacement, is relatively insensitive to the force and moment on the deck during the vertical vibration, but both Y_c and θ_c are strongly locked-in with the lift and moment exerted on the deck resulting from the vortex formation behind the deck. These phase relations among Y_c, θ_c, C_{L_s} and C_{M_s} during the torsional vibration are closely related to the vortex formation around the deck, as shown in figure 12. Note that this vortex-formation frequency ($f_{vf}h/U = 0.025$) is very different from the natural vortex-shedding frequency around the stationary deck. As Y_c and θ_c become negative ($tU/h = 676$), flow separates from the upper edge of the left fence and a large vortex is formed there, creating low pressure on the upper surface of the deck, resulting in positive lift and negative moment. As Y_c and θ_c are negatively maximum ($tU/h = 685$), the lift is maximum and the moment is nearly zero. As the vortex formed above the upper surface travels toward the right part of the upper surface, positive moment is generated. Accordingly, the deck rotates counterclockwise (e.g. at $tU/h = 688$). When $\theta_c > 0$, flow separation occurs at the lower edge of the left fence and a large vortex forms there, creating low pressure on the lower surface of the deck, resulting in negative lift and positive moment. Then, a process similar to that described above proceeds. This result clearly indicates that the torsional vibration is an aeroelastic fluttering (Scanlan 1982; Billah & Scanlan 1991).

The time traces of the total energy accumulated in the TNB are shown in figure 13, together with those containing Y_c and its derivatives (E_{Y_c}) or θ_c and its derivatives (E_{θ_c}) in

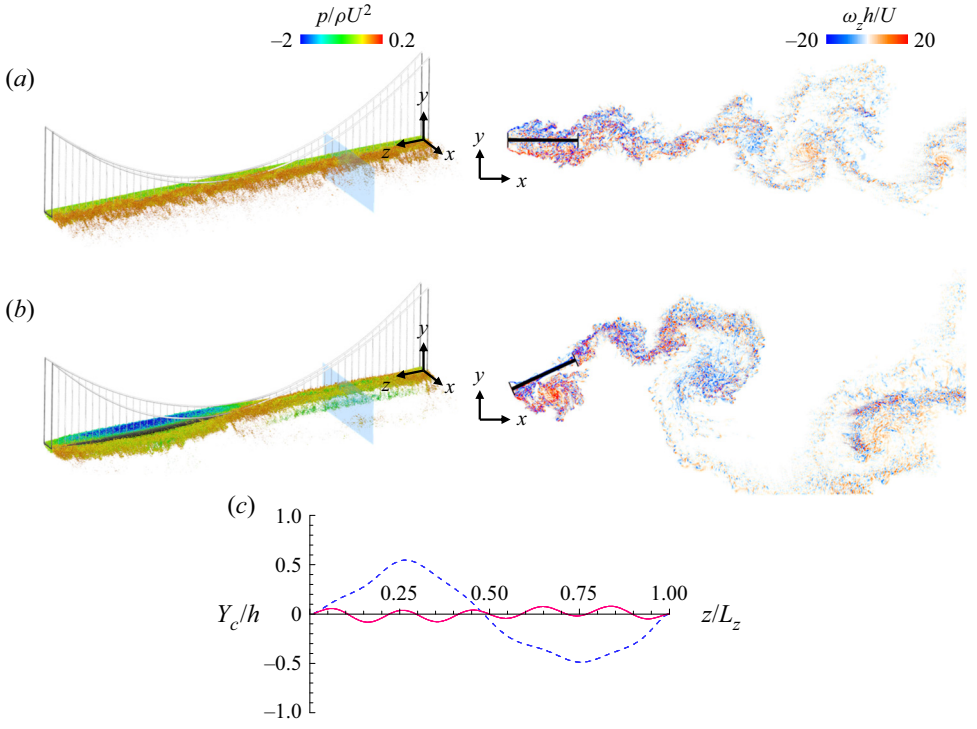

Figure 10. Instantaneous three-dimensional vortical structures (iso-surfaces of $\lambda_2 = -20$; Jeong & Hussain 1995) coloured with the contours of the instantaneous pressure (left), and contours of the instantaneous spanwise vorticity at $z = L_z/4$ (denoted as rectangular planes on the left) (right): (*a*) $tU/h = 354$ (vertical vibration); (*b*) $tU/h = 746$ (torsional vibration). (*c*) Y_c vs z at $tU/h = 354$ (———, red) and 746 (– – – – –, blue). Note that the bridge is scaled by 1/5 in the z direction in (*a*,*b*).

(2.6)–(2.10), where

$$E_{Y_c} = \frac{M}{2}\int_0^{L_z} Y_{c_t}^2\,\mathrm{d}z + m\int_0^{L_z} Y_{c_t}^2\xi\,\mathrm{d}z + Mg\int_0^{L_z} Y_c\,\mathrm{d}z + 2mg\int_0^{L_z} Y_c\xi\,\mathrm{d}z + \frac{EI}{2}\int_0^{L_z} Y_{c_{zz}}^2\,\mathrm{d}z + 2H_0\int_0^{L_z}\xi\left(\sqrt{1+(s'+Y_{c_z})^2}-\sqrt{1+s'^2}\right)\mathrm{d}z + \frac{AE}{L_c}\left(\int_0^{L_z}\sqrt{1+(s'+Y_{c_z})^2}\,\mathrm{d}z - L_c\right)^2, \tag{3.2}$$

$$E_{\theta_c} = \frac{M}{6}\int_0^{L_z} l^2\theta_{c_t}^2\,\mathrm{d}z + m\int_0^{L_z} l^2\theta_{c_t}^2\xi\,\mathrm{d}z + \frac{GK}{2}\int_0^{L_z}\theta_{c_z}^2\,\mathrm{d}z + H_0\int_0^{L_z}\xi\left(\sqrt{1+(s'-l\theta_{c_z})^2}-\sqrt{1+s'^2}\right)\mathrm{d}z + \frac{AE}{2L_c}\left(\int_0^{L_z}\sqrt{1+(s'-l\theta_{c_z})^2}\,\mathrm{d}z - L_c\right)^2$$

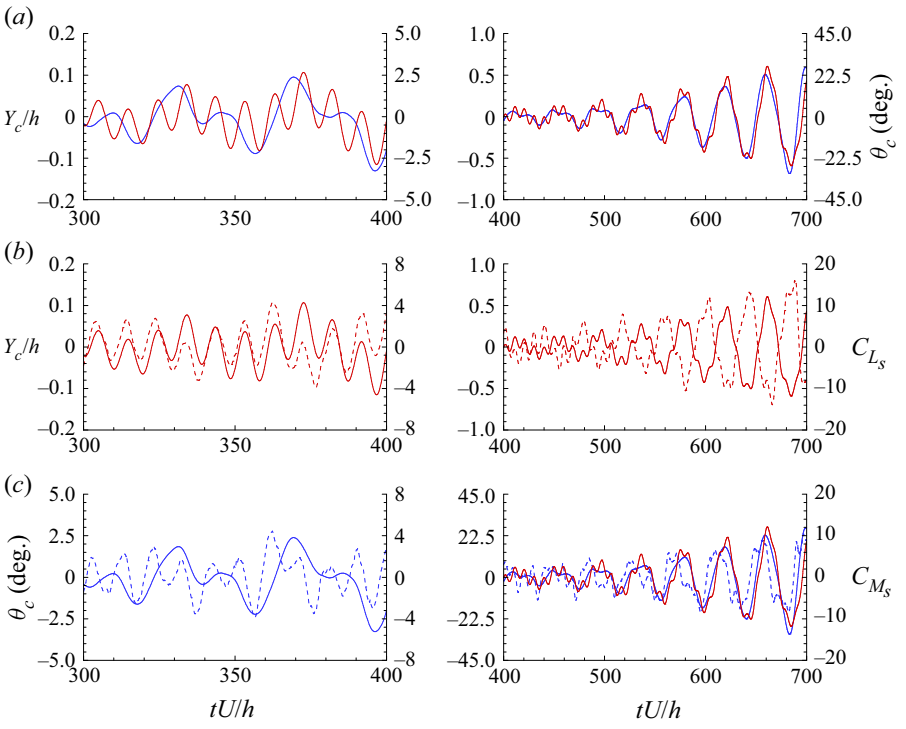

Figure 11. Time traces of the vertical displacement, rotational angle and sectional lift and moment coefficients at $z = L_z/4$: (*a*) Y_c (———, red) vs θ_c (———, blue); (*b*) Y_c (———, red) vs C_{L_s} (– – – – –, red); (*c*) θ_c (———, blue) vs C_{M_s} (– – – – –, blue). On the right figure of (*c*), Y_c (———, red) is also added to show the phase differences from θ_c and C_{M_s}. Note that the scales of the *y*-axes are different between the left and right figures.

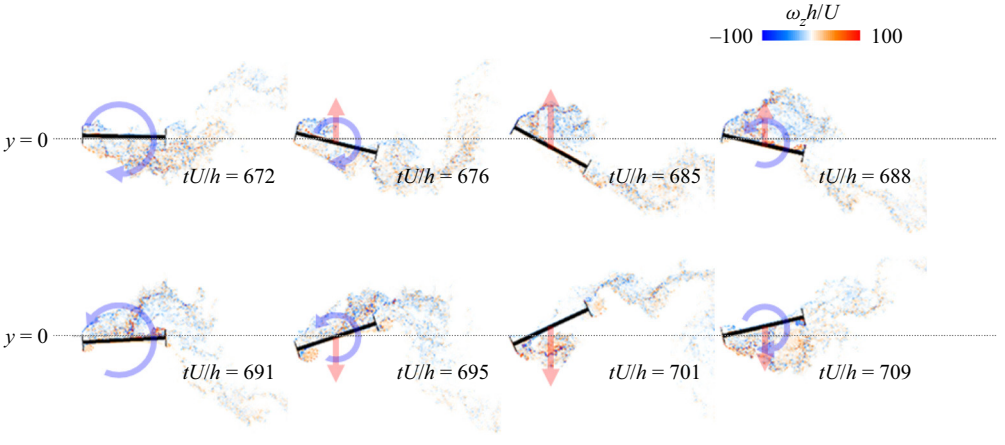

Figure 12. Motion of the deck at $z = L_z/4$ during the torsional vibration and its relation with the sectional lift and moment exerted on the deck, together with the contours of the instantaneous spanwise vorticity. Here, the scarlet- and light-blue-coloured arrows indicate relative magnitudes of the sectional lift and moment, respectively.

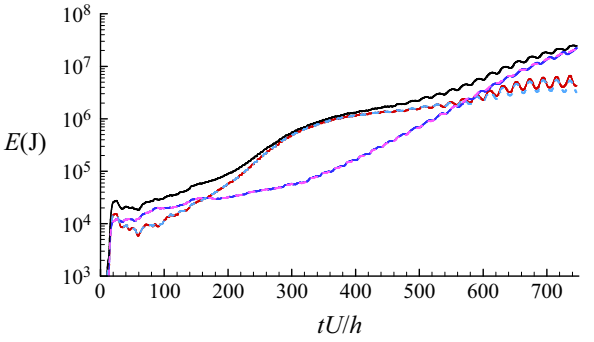

Figure 13. Time traces of the energy accumulated in the TNB: ——— (black), total energy (sum of (2.6)–(2.10)); ——— (red), E_{Y_c} (energy containing Y_c and its derivatives only); ——— (blue), E_{θ_c} (energy containing θ_c and its derivatives only); – – – – – (SkyBlue), E_{L,Y_c}; – – – – – (VioletRed), E_{M,θ_c}.

$$+ H_0 \int_0^{L_z} \xi \left(\sqrt{1 + (s' + l\theta_{c_z})^2} - \sqrt{1 + s'^2} \right) \mathrm{d}z$$
$$+ \frac{AE}{2L_c} \left(\int_0^{L_z} \sqrt{1 + (s' + l\theta_{c_z})^2}\, \mathrm{d}z - L_c \right)^2. \tag{3.3}$$

At very early time ($tU/h < 165$), E_{Y_c} is smaller than E_{θ_c}, and becomes larger than E_{θ_c} at $165 < tU/h < 570$. The growth rate of E_{θ_c} is much bigger than that of E_{Y_c} at $tU/h > 350$; E_{θ_c} becomes bigger than E_{Y_c} at $tU/h > 570$, and the total energy in the TNB is mainly determined by the torsional vibration at this time period. On the other hand, the growth rate of E_{Y_c} suddenly decreases at $tU/h \approx 350$ and E_{Y_c} shows a limited amplitude growth unlike E_{θ_c}. This behaviour is very similar to that of $|a_{n_m=10}|$ of Y_c (figure 8(*a*); cases with $Y_c \equiv 0$ or $\theta_c \equiv 0$ are separately simulated and their results are given in § 3.3, where further discussions are made). Note that, in the absence of the free-stream velocity, the threshold energy level above which the vertical vibration changed into the torsional vibration was 82.1 MJ for $n_m = 10$ according to Arioli & Gazzola (2017). However, as shown in figure 13, the torsional vibration starts even with a much lower energy level ($E_{Y_c} = 846$ kJ at $tU/h = 350$) in the presence of the free-stream velocity (or with fluid–structure interaction).

In figure 13, we also compare E_{Y_c} and E_{θ_c} with E_{L,Y_c} and E_{M,θ_c} (energy accumulated in the bridge by the aerodynamic lift and moment, respectively), where E_{L,Y_c} and E_{M,θ_c} are defined as

$$E_{L,Y_c}(t) = \int_0^t \int_0^{L_z} Y_{c_t}(z,t) L_s(z,t)\, \mathrm{d}z\, \mathrm{d}t, \tag{3.4}$$

$$E_{M,\theta_c}(t) = \int_0^t \int_0^{L_z} \theta_{c_t}(z,t) M_s(z,t)\, \mathrm{d}z\, \mathrm{d}t. \tag{3.5}$$

The energy accumulated in the TNB by the aerodynamic force and moment are very similar to E_{Y_c} and E_{θ_c}, respectively, verifying that the sources of the vertical and torsional vibrations are indeed the aerodynamic lift and moment, respectively.

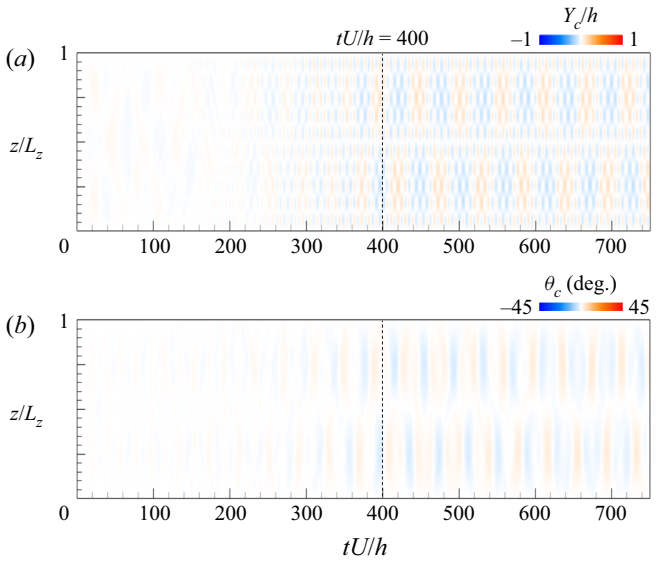

Figure 14. Temporal behaviours of the vertical displacement and rotational angle when the fluid flow is removed at $tU/h \geq 400$: (*a*) Y_c; (*b*) θ_c. Here, the maximum values of Y_c/h and θ_c at $tU/h = 750$ are 0.13 and 3.6°, respectively.

3.3. *Further study of the vertical and torsional vibrations*

In this section, we perform a few more numerical simulations to obtain the critical flutter wind speed and investigate the roles of the free-stream velocity and vertical vibration in the growth of the torsional vibration. Figure 14 shows the temporal behaviours of Y_c and θ_c when the fluid flow is removed at $tU/h \geq 400$ (i.e. only (2.3) and (2.4) without the aerodynamic terms containing C_{L_s} and C_{M_s} being solved). The amplitudes and wavelengths of Y_c and θ_c do not change in time, unlike those in figure 6. This result indicates that the presence of fluid flow or fluid–structure interaction is required for the transition to torsional vibration, when the energy of the vertical vibration is not sufficiently high. To see if the existence of the vertical vibration is required for the initiation of the torsional vibration even in the presence of fluid flow, we perform two additional simulations with $Y_c \equiv 0$ (i.e. no vertical displacement is allowed) or $\theta_c \equiv 0$ (i.e. no angular displacement is allowed) in the presence of the free-stream velocity, and their results are shown in figure 15. Even without vertical vibration, the torsional vibration with $\lambda_z = L_z$ ($n_m = 2$) occurs, and the energy growth rate is slightly lower than that of the natural case (figure 13), suggesting that the vertical vibration is not a necessary condition for the occurrence and rapid growth of the torsional vibration in the presence of fluid flow. Meanwhile, we observed in figure 13 that the growth of the vertical displacement becomes slow during the torsional vibration as compared with that of the angular displacement. Whether this slow growth of Y_c is due to the occurrence of the torsional vibration or not, the growth of the vertical displacement with $\theta_c \equiv 0$ (in the absence of the angular displacement) is shown in figures 15(*b*) and 15(*c*). The vertical vibration with the same wavelength ($n_m = 10$) and frequency ($fh/U = 0.103$) as those of the natural case evolves after an early transition period, and the energy of Y_c is saturated at $tU/h > 400$ at a lower magnitude than that of the natural case. In general, lock-in is not necessarily induced by resonance, and can arise from instability of the structure (De Langre 2006; Zhang *et al.* 2015; Gao *et al.* 2017). However, the present result suggests that the slow growth of Y_c

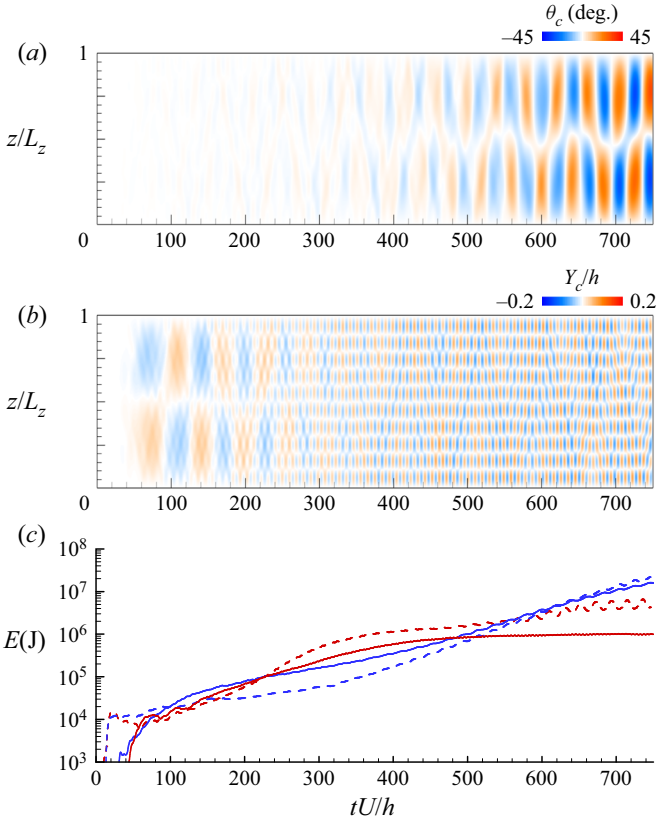

Figure 15. Temporal behaviours of the angular and vertical displacements and energy ($Y_c \equiv 0$ or $\theta_c \equiv 0$): (*a*) θ_c with $Y_c \equiv 0$; (*b*) Y_c with $\theta_c \equiv 0$; (*c*) energy (——— (blue), E_{θ_c} ($Y_c \equiv 0$); ——— (red), E_{Y_c} ($\theta_c \equiv 0$); – – – – – (blue), E_{θ_c} (natural case); – – – – – (red), E_{Y_c} (natural case)).

is not directly caused by the occurrence of torsional vibration, and the vertical vibration itself does not evolve into fluttering even in the presence of fluid flow but only experiences the resonance-induced lock-in.

So far, we have shown that the torsional vibration grows exponentially at $U = 18$ m s^{-1} ($Re = 10\,000$) even if the vertical displacement is set to zero, but it does not grow in the absence of the free-stream velocity when the energy of the vertical displacement is not sufficiently high. On the other hand, it was shown by Arioli & Gazzola (2017) that the torsional vibration suddenly increases in the absence of the free-stream velocity when the initial vertical displacement is large enough. From these results, one can expect that there must be a critical free-stream velocity from which the torsional vibration rapidly grows under zero initial vertical displacement. To see if the torsional vibration does not grow at a lower free-stream velocity, we perform a few more simulations at $U = 9$, 8, 6 and 2.25 m s^{-1}, respectively, corresponding to $Re \approx 5000$, 4444, 3333 and 1250. The temporal evolutions of E_{θ_c} and E_{Y_c} for different free-stream velocities are shown in figure 16. At $U \geq 9$ m s^{-1}, E_{θ_c} grows exponentially and is bigger than E_{Y_c}, indicating that the torsional vibration is dominant. On the other hand, at $U \leq 8$ m s^{-1}, E_{θ_c} and E_{Y_c} are saturated and E_{θ_c} is much smaller than E_{Y_c}, indicating that the vertical vibration is dominant (for example, the maximum angular displacement is less than 1 degree for $U = 8$ m s^{-1}). Since the natural frequency of the torsional mode ($n_m = 2$) is

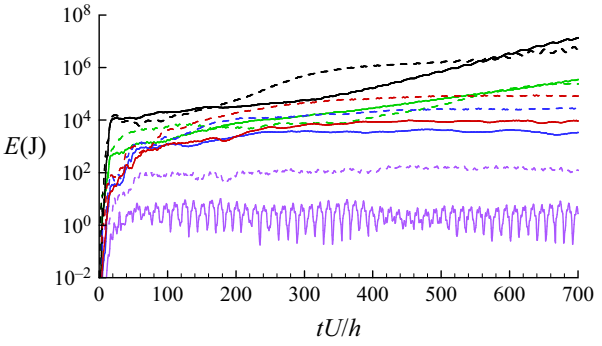

Figure 16. Comparison of E_{θ_c} and E_{Y_c} for different free-stream velocities: black lines, $U = 18$ m s^{-1}; green lines, $U = 9$ m s^{-1}; red lines, $U = 8$ m s^{-1}; blue lines, $U = 6$ m s^{-1}; purple lines, $U = 2.25$ m s^{-1}. Here, solid and dashed lines are for E_{θ_c} and E_{Y_c}, respectively.

$f_{nat} = 0.025U/h = 0.1875$ Hz (figure 4*b*) and $B = 2l = 5h = 12$ m in the present study, the non-dimensional critical flutter wind speed obtained from the present study is $3.56 < U_c/(f_{nat}B) \leq 4$, where $U_c/(f_{nat}B) = 3.56$ and 4 correspond to $U = 8$ and 9 m s^{-1}, respectively. This result agrees very well with the previous ones: i.e. $U_c/(f_{nat}B) = 4$ by Matsumoto, Shirato & Hirai (1992), 3.55 by Scanlan (1999), 3.6–4 (instability analysis) and 4 (numerical simulation) by Larsen (2000), 4 by Szabó *et al.* (2020) and 3.5–4.4 by Hu *et al.* (2022). It is also noteworthy that Ammann *et al.* (1941) obtained $U_c/(f_{nat}B) = 4$ for a two-dimensional H-section (wind tunnel test), but failed to obtain a reasonable critical wind speed for a 1 : 234 scale full model of the TNB.

The lowest Reynolds number at which vortex shedding occurs behind a stationary deck cross-section is obtained as $Re_{cr} = 89$ by performing additional two-dimensional simulations. It has been reported that a vortex-induced vibration (VIV) may occur even in the sub-critical regime where no vortex shedding exists for stationary structures (Cossu & Morino 2000; Mittal & Singh 2005; Kou *et al.* 2017). Whether a similar phenomenon occurs for the present TNB, we perform two additional simulations at $Re = 75$ and 50. For both Reynolds numbers, the maximum vertical and angular displacements, Y_c/h and θ_c, are less than 2×10^{-6} and $10^{-4\circ}$, respectively, indicating that VIV does not occur at these sub-critical Reynolds numbers for the TNB.

4. Conclusions

The vertical vibration and transition to torsional vibration of the TNB were examined by large-scale three-dimensional direct numerical simulation using 13.4 billion grid points and maximum 160 000 MPI processes. Real-scale structural parameters of the bridge were used for the simulation, and the vertical (Y_c) and rotational (θ_c) displacements of the deck centre were observed to investigate the vertical and torsional motions of the bridge. The Reynolds number based on the free-stream velocity and height of the deck fence was lower ($Re = 10\,000$) than the actual one on the day of the collapse ($Re = 3.06 \times 10^6$), but the magnitudes of fluid properties were adjusted to provide the real-scale aerodynamic force and moment on the bridge deck. Fluid–structure interaction of the wind and bridge was also employed. The wavelengths and frequencies of the vertical and torsional vibrations showed good agreement with the recorded data of the incident.

The natural frequency of the vertical vibration ($f_{nat}h/U = 0.1$–0.105) with a wavelength of $\lambda_z = L_z/5$ was very similar to the vortex-shedding frequency of the flow over a

stationary deck ($f_{vs}h/U = 0.111$), which indicated that the vertical vibration was induced by the lock-in with the vortex shedding. After the saturation of the vertical vibration, a torsional vibration started and grew exponentially in time. During the vertical vibration, the vertical displacement was in phase with the sectional aerodynamic lift (but not with the rotational angle). However, during the torsional vibration, the vertical displacement and rotational angle of the deck were closely associated with the fluid flow, i.e. the vertical displacement was in phase with the rotational angle, 180° out of phase with the sectional aerodynamic lift and 90° out of phase with the sectional aerodynamic moment. The transition from the vertical to torsional vibration was indicated by suggesting a new non-dimensional variable Δ by comparing the relative strength of the vertical to torsional vibrations. The magnitudes of the energy from the vertical and angular displacements mostly consisted of the energy accumulated by the aerodynamic lift and moment, respectively, indicating close interaction between the bridge and fluid flow. Initially, the energy containing the vertical displacement exponentially grew in time and then became saturated. After the saturation of the vertical displacement energy, the energy of the angular displacement grew exponentially in time and became much larger than that of the vertical displacement. By testing a few more free-stream velocities, we showed that the critical flutter wind speed is $3.56 < U_c/(f_{nat}B) \leq 4$, where f_{nat} is the natural frequency of the torsional vibration, and B is the deck cross-section width. This critical wind speed agreed very well with those by previous studies (Ammann *et al.* 1941; Matsumoto *et al.* 1992; Scanlan 1999; Larsen 2000; Szabó *et al.* 2020; Hu *et al.* 2022).

We also showed that the presence of fluid flow is required for the development of the torsional vibration, when the vertical vibration energy is not sufficiently high. For example, the energy accumulated in Y_c and θ_c (E_{Y_c} and E_{θ_c}, respectively) revealed that the torsional vibration sufficiently grows even with $E_{Y_c} = 846$ kJ at $tU/h = 350$, which is much lower than the energy threshold of instability (82.1 MJ) of the vertical mode ($n_m = 10$) in the absence of the free-stream velocity suggested by Arioli & Gazzola (2017). The vortex-formation frequency during the torsional vibration was significantly different from the natural vortex-shedding frequency behind the stationary TNB deck, and the energy accumulated by the aerodynamic lift and moment matched well with E_{Y_c} and E_{θ_c}, respectively, meaning that the torsional instability occurs through the aeroelastic fluttering. Apart from the real vibration process during the collapse of the TNB in 1940, we conducted a simulation by setting a zero vertical displacement. The torsional vibration still developed through a large-amplitude aerodynamic fluttering even in the absence of the vertical vibration.

Finally, we would like to mention two approximations made in the present study. One is that the structural damping effect was neglected in the present nonlinear structure model (Arioli & Gazzola 2017), and thus the energy growth might be over-predicted. Introducing the damping effect may reduce the natural frequencies of the vertical and torsional modes and delay their growth, but the essential vibration patterns are not expected to change significantly. The second is that we used a much lower Reynolds number than the real one in 1940. Thus, there exist some effects from small-scale turbulence that was not resolved in the present simulation, but we expect that the force and moment generated by those small scales have no significant effect on the TNB vibration motion.

Funding. This work was supported by the Korea Institute of Science and Technology Information (P20015), the National Supercomputing Center with supercomputing resources including technical support (KSC-2020-CHA-0005) and the National Research Foundation through the Ministry of Science and ICT (2019R1A2C2086237 and 2022R1A2B5B02001586).

Declaration of interests. The authors report no conflict of interest.

Author ORCIDs.
Haecheon Choi https://orcid.org/0000-0003-0696-847X.

References

Abbas, T., Kavrakov, I. & Morgenthal, G. 2017 Methods for flutter stability analysis of long-span bridges: a review. *Proc. Inst. Civil Engrs: Bridge Engng* **170** (4), 271–310.

Adekanye, O. & Washington, T. 2018 Nonstandard finite difference scheme for a Tacoma Narrows Bridge Model. *Appl. Math. Model.* **62**, 223–236.

Ammann, O.H., von Kármán, T. & Woodruff, G.B. 1941 The failure of the Tacoma Narrows Bridge: a report to the Honorable John M. Carmody, Administrator, Federal Works Agency, Washington, DC. Board of Engineers.

Arioli, G. & Gazzola, F. 2015 A new mathematical explanation of what triggered the catastrophic torsional mode of the Tacoma Narrows Bridge. *Appl. Math. Model.* **39** (2), 901–912.

Arioli, G. & Gazzola, F. 2017 Torsional instability in suspension bridges: the Tacoma Narrows Bridge case. *Commun. Nonlinear Sci. Numer. Simul.* **42**, 342–357.

Berchio, E. & Gazzola, F. 2015 A qualitative explanation of the origin of torsional instability in suspension bridges. *Nonlinear Anal. Theory Meth. Applics.* **121**, 54–72.

Billah, K.Y. & Scanlan, R.H. 1991 Resonance, Tacoma Narrows bridge failure, and undergraduate physics textbooks. *Am. J. Phys.* **59** (2), 118–124.

Choi, H. & Moin, P. 1994 Effects of the computational time step on numerical solutions of turbulent flow. *J. Comput. Phys.* **113** (1), 1–4.

Chung, J. & Hulbert, G.M. 1993 A time integration algorithm for structural dynamics with improved numerical dissipation: the generalized-α method. *J. Appl. Mech.* **60** (2), 371–375.

Cossu, C. & Morino, L. 2000 On the instability of a spring-mounted circular cylinder in a viscous flow at low Reynolds numbers. *J. Fluids Struct.* **14** (2), 183–196.

De Langre, E. 2006 Frequency lock-in is caused by coupled-mode flutter. *J. Fluids Struct.* **22** (6–7), 783–791.

Den Hartog, J.P. 1985 *Mechanical Vibrations*. Dover Publications.

Gao, C., Zhang, W., Li, X., Liu, Y., Quan, J., Ye, Z. & Jiang, Y. 2017 Mechanism of frequency lock-in in transonic buffeting flow. *J. Fluid Mech.* **818**, 528–561.

Green, D. & Unruh, W.G. 2006 The failure of the Tacoma Bridge: a physical model. *Am. J. Phys.* **74** (8), 706–716.

Hu, C., Zhao, L. & Ge, Y. 2022 Wind-induced instability mechanism of Old Tacoma Narrows Bridge from aerodynamic work perspective. *J. Bridge Engng* **27** (5), 04022029.

Jeong, J. & Hussain, F. 1995 On the identification of a vortex. *J. Fluid Mech.* **285**, 69–94.

Jin, D., Wu, Z. & Choi, H. 2021 A predictive model of the drag coefficient of a circular cylinder. *Phys. Fluids* **33** (11), 111702.

von Kármán, T. & Edson, L. 1967 *The Wind and Beyond: Theodore von Kármán, Pioneer in Aviation and Pathfinder in Space*. Little, Brown & Co..

Kim, K., Baek, S.-J. & Sung, H.J. 2002 An implicit velocity decoupling procedure for the incompressible Navier–Stokes equations. *Intl J. Numer. Meth. Fluids* **38** (2), 125–138.

Kim, W. & Choi, H. 2019 Effect of the spanwise computational domain size on the flow over a two-dimensional bluff body with spanwise periodic perturbations at low Reynolds number. *Comput. Fluids* **183**, 102–106.

Kim, K.-H., Kang, J.-H., Pan, X. & Choi, J.-I. 2021 PaScal_TDMA: a library of parallel and scalable solvers for massive tridiagonal systems. *Comput. Phys. Commun.* **260**, 107722.

Kim, J., Kim, D. & Choi, H. 2001 An immersed-boundary finite-volume method for simulations of flow in complex geometries. *J. Comput. Phys.* **171** (1), 132–150.

Kim, W., Lee, J. & Choi, H. 2016 Flow around a helically twisted elliptic cylinder. *Phys. Fluids* **28** (5), 053602.

Kim, W., Lee, I. & Choi, H. 2018 A weak-coupling immersed boundary method for fluid-structure interaction with low density ratio of solid to fluid. *J. Comput. Phys.* **359**, 296–311.

Kou, J., Zhang, W., Liu, Y. & Li, X. 2017 The lowest Reynolds number of vortex-induced vibrations. *Phys. Fluids* **29** (4), 041701.

Kwon, O.-K., Lee, J., Lee, J., Kang, J.-H & Choi, J.-I. 2020 MPI parallel implementation for pseudo-spectral simulations for turbulent channel flow. *Intl J. Comput. Fluid Dyn.* **34** (7–8), 569–582.

Lacarbonara, W. 2013 *Nonlinear Structural Mechanics: Theory, Dynamical Phenomena and Modeling*. Springer Science & Business Media.

LARSEN, A. 2000 Aerodynamics of the Tacoma Narrows Bridge – 60 years later. *Struct. Engng Intl* **10** (4), 243–248.

MATSUMOTO, M., SHIRATO, H. & HIRAI, S. 1992 Torsional flutter mechanism of 2-D H-shaped cylinders and effect of flow turbulence. *J. Wind Engng Ind. Aerodyn.* **41** (1-3), 687–698.

MCKENNA, P.J. 1999 Large torsional oscillations in suspension bridges revisited: fixing an old approximation. *Am. Math. Mon.* **106** (1), 1–18.

MITTAL, S. & SINGH, S. 2005 Vortex-induced vibrations at subcritical *Re*. *J. Fluid Mech.* **534**, 185–194.

OLSON, D.W., WOLF, S.F. & HOOK, J.M. 2015 The Tacoma Narrows Bridge collapse. *Phys. Today* **68** (11), 64–65.

PAULEY, L.L., MOIN, P. & REYNOLDS, W.C. 1990 The structure of two-dimensional separation. *J. Fluid Mech.* **220**, 397–411.

SCANLAN, R.H. 1982 Developments in low-speed aeroelasticity in the civil engineering field. *AIAA J.* **20** (6), 839–844.

SCANLAN, R.H. 1999 Estimates of skew wind speeds for bridge flutter. *J. Bridge Engng* **4** (2), 95–98.

SCANLAN, R.H. & TOMKO, J.J. 1971 Airfoil and bridge deck flutter derivatives. *J. Engng Mech.* **97** (6), 1717–1737.

SCHEW, G. 2013 Reynolds-number-effects in flow around a rectangular cylinder with aspect ratio 1:5. *J. Fluids Struct.* **39**, 15–26.

SERWAY, R.A. & JEWETT, J.W. 2018 *Physics for Scientists and Engineers*, 10th edn. Cengage Learning.

SZABÓ, G., GYÖRGYI, J. & KRISTÓF, G. 2020 Three-dimensional FSI simulation by using a novel hybrid scaling–application to the Tacoma Narrows Bridge. *Period Polytech. Chem. Engng* **64** (4), 975–988.

WHITE, F.M. 2016 *Fluid Mechanics*, 8th edn. McGraw-Hill.

YAKUBOVICH, V.A. & STARZHINSKII, V.M. 1975 *Linear Differential Equations with Periodic Coefficients*. John Wiley and Sons.

ZHANG, W., DOU, Z. & GAO, C. 2020 Various flow-induced vibrations of bridges and von Kármán vortex street. *Acta Aerodyn. Sin.* **38** (3), 405–412.

ZHANG, W., LI, X., YE, Z. & JIANG, Y. 2015 Mechanism of frequency lock-in in vortex-induced vibrations at low Reynolds numbers. *J. Fluid Mech.* **783**, 72–102.